# PIC Simulation of Energetic-ion Injection Effects on Nonlinear Development of Lower Hybrid Wave Instabilities

Tsubasa Kotani[1], Mieko Toida[2], Toseo Moritaka[2], and Satoshi Taguchi[1]

[1]*Graduate School of Science, Kyoto University, Sakyoku, Kyoto 606-8502, Japan*
[2]*National Institute for Fusion Science, Toki, Gifu 509-5202, Japan*

By means of one-dimensional, electromagnetic, particle-in-cell simulations, we investigate the nonlinear development of lower hybrid wave (LHW) instabilities driven by energetic ions with a ring-like velocity distribution, paying special attention to the effects of energetic-ion injection. We consider the LHWs propagating perpendicular to the magnetic field in a collisionless plasma into which energetic ions with a speed smaller than the Alfvén speed are continuously injected. We found that the LHWs excited by the energetic ions can maintain large amplitudes for a long time because the continuous injection causes the steep gradient of the energetic-ion velocity distribution. Furthermore, as time advances, the wavenumber of excited modes become larger. Because of this nonlinear development of the LHWs, the energy transfer from the energetic ions to bulk ions through the LHWs is enhanced. As the injection speed increases, a wide wavenumber range of the modes are excited and the bulk-ion energy change increases.

## 1. Introduction

Energetic ions with a ring-like velocity distribution in the velocity space perpendicular to the magnetic field are often produced in fusion and space plasmas. In fusion plasmas, such energetic ions can be generated by neutral beam injection for plasma heating and by nuclear fusion reaction. In the Earth's magnetosphere, ion ring-like velocity distributions are observed near the bow shock[1)] and in the inner magnetosphere.[2)] The ion ring-like velocity distribution can cause various wave instabilities,[3)] depending on factors such as the wave propagation direction, the energetic-ion speed, the plasma density, and the magnetic field strength.

The ring-like energetic ions excite electromagnetic fast magnetosonic waves when the energetic-ion ring speed is greater than the Alfvén speed. In the inner magnetosphere, the fast magnetosonic waves are considered to contribute to the acceleration of radiation belt electrons[4–8)] and cold ions.[9,10)] When the energetic-ion ring speed is much smaller than the

Alfvén speed, electrostatic lower hybrid waves (LHWs) are excited.[11,12] Here, we define the LHWs as electrostatic waves around the lower hybrid resonance frequency $\omega_{LH}$, which is given by

$$\omega_{LH}^2 = (\Omega_i \Omega_e)^2 \frac{1 + \omega_{pi}^2/\Omega_i^2}{\omega_{pe}^2 + \Omega_e^2}, \tag{1}$$

where $\Omega_i$ and $\Omega_e$ are the ion and electron cyclotron frequencies, and $\omega_{pi}$ and $\omega_{pe}$ are the ion and electron plasma frequencies, respectively. The LHWs are often observed in fusion[13] and space plasmas.[14] Since the LHWs can also accelerate both ions and electrons, increasing attention has been paid to the LHW instabilities, for example, in association with solar flares.[15–17] In the auroral region of the Earth's magnetosphere, the LHWs excited by precipitating ions can contribute to the energization of oxygen ions.[18] Nonlinear coupling between the LHWs and other waves[19–22] and mode conversion from the LHWs to other waves[23,24] have also been important research subjects.

Particle-in-cell (PIC) simulation is a useful tool for studying the nonlinear evolution of the LHW instabilities driven by the ring-like energetic ions. Most of the simulation studies solve initial value problems,[7,8,12,15–17,19,21,22] where the ring-like energetic ions are set up at the initial time, $t = 0$, and the relaxation of the energetic-ion velocity distribution is simulated. However, in the real situation, the continuous injection or loss of the energetic ions occurs even after $t = 0$, which had not been considered in previous studies. For example, in the fusion plasmas, the energetic ions are continuously generated by the neutral beam injection for plasma heating. Interactions between the solar wind and the Earth's magnetosphere can cause the continuous injection of energetic ions into the inner magnetosphere.[25]

The continuous injection of these energetic ions leads to the reshaping of the velocity distribution, which can significantly affect the nonlinear development of the instabilities. Therefore, the initial value problem is not sufficient to investigate the long-time evolution of the instabilities, and the PIC simulations including the injection and loss of the energetic ions are required.

In this paper, we study the LHW instabilities driven by continuous energetic-ion injection using one-dimensional, electromagnetic, PIC simulations. We show that the energetic-ion injection significantly affects the nonlinear development of the instabilities and associated energy transfer from energetic ions to bulk ions.

In Sect. 2, we describe the linear theory of the LHW instabilities driven by the ring-like energetic ions with a ring speed much smaller than the Alfvén speed. In Sect. 3, we present the simulation method and parameters. In Sect. 4, we show the simulation results of

an initial value problem and an injection model where the density of the energetic ions is zero at the initial time $t = 0$ and then increases with time. The comparison between the two results reveals the effects of the energetic-ion injection on the nonlinear development of the LHW instabilities and associated energy transfer. In Sect. 5, we discuss how the nonlinear development of the LHW instabilities depends on the energetic-ion injection speed. Section 6 gives a summary of our work.

## 2. Linear Theory

Before showing the simulation results, we describe the linear theory for LHW instabilities driven by ring-like energetic ions. We consider waves propagating exactly perpendicular to the magnetic field in a uniform plasma. The plasma consists of electrons, bulk ions, and the energetic ions. The velocity distributions of the bulk ions and the electrons are Maxwellian,

$$f_{s0}(v_\parallel, v_\perp) = \frac{1}{(2\pi v_{Ts}^2)^{3/2}} \exp\left(-\frac{v_\parallel^2 + v_\perp^2}{2v_{Ts}^2}\right), \tag{2}$$

where the subscript $s$ denotes ion ($s = i$) or electron ($s = e$), the subscripts $\parallel$ and $\perp$ denote parallel and perpendicular to the background magnetic field, respectively, and $v_{Ts}$ is the thermal velocity. The energetic ions have a ring-like velocity distribution with a finite width,

$$f_{h0}(v_\parallel, v_\perp) = \frac{1}{4\pi^2 u_\perp v_{Th}^2} \exp\left(-\frac{(v_\perp - u_\perp)^2 + v_\parallel^2}{2v_{Th}^2}\right), \tag{3}$$

where $v_{Th}$ is the thermal velocity of the energetic ions and $u_\perp$ is the perpendicular ring speed of the energetic ions. Note that Eq. (3) is valid when $u_\perp^2 \gg v_{Th}^2$. In the limit of $v_{Th} \to 0$, Eq. (3) reduces to the cold ring-like velocity distribution, $f_{h0} \propto \delta(v_\perp - u_\perp)\delta(v_\parallel)$.

In this situation, the longitudinal dielectric permittivity $\epsilon_L$ is given by[3)]

$$\epsilon_L = 1 + \sum_{s=i,j,h} \frac{\omega_{ps}^2}{k_\perp^2} \sum_{n=-\infty}^{\infty} \int d^2v \frac{n\Omega_s}{v_\perp} \frac{\partial f_{s0}}{\partial v_\perp} \frac{J_n^2(\xi)}{\omega - n\Omega_s}, \tag{4}$$

where $n$ is an integer, $d^2v = dv_\parallel dv_\perp 2\pi v_\perp$, $J_n$ is the Bessel function of the order $n$, and $\xi = k_\perp v_\perp/\Omega_s$. We rewrite $\epsilon_L$ as

$$\epsilon_L = \epsilon_{main} + \epsilon_h, \tag{5}$$

where $\epsilon_{main}$ is the term of the bulk ions and the electrons, and $\epsilon_h$ is the term of the energetic ions. Using the cold approximation, we can write the main term of Eq. (5) as

$$\epsilon_{main} = \left(1 + \frac{\omega_{pe}^2}{\Omega_e^2}\right)\left(1 - \frac{\omega_{LH}^2}{\omega^2}\right). \tag{6}$$

Since we are interested in the waves with the frequency $\omega \simeq \omega_{LH} \simeq n\Omega_i$, we assume that in the summation for the energetic ions of Eq. (4), the terms other than the $n$-th term can be

neglected. Therefore, the energetic-ion term of Eq. (5) is written as[3)]

$$\epsilon_h = \frac{\omega_{ph}^2}{k_\perp^2} \int dv_\perp 2\pi v_\perp \left(\frac{n\Omega_i}{v_\perp}\right) \frac{\partial f_{h\perp}}{\partial v_\perp} \frac{J_n^2(\xi)}{\omega - n\Omega_i} \tag{7}$$

$$= -\frac{\omega_{ph}^2}{\Omega_i} \frac{2n}{\omega - n\Omega_i} D_{IM}, \tag{8}$$

where $f_{h\perp}(v_\perp) = \int f_{h0}(v_\parallel, v_\perp) dv_\parallel$ is the perpendicular velocity distribution of the energetic ions and $D_{IM}$ is defined as

$$D_{IM} \equiv \int dv_\perp 2\pi v_\perp f_{h\perp} \frac{J_n(\xi) J_n'(\xi)}{\xi}, \tag{9}$$

with $J_n'(\xi) = dJ_n(\xi)/d\xi$.

We write the solution of $\epsilon_{main} + \epsilon_h = 0$ as $\omega = \omega_r + \Delta$. Assuming $\omega_r \simeq \omega_{LH} \simeq n\Omega_i$, we derive the representation of $\Delta$ as

$$\frac{\Delta^2}{\Omega_i^2} = \frac{1}{1 + \omega_{pe}^2/\Omega_e^2} \frac{\omega_{ph}^2 \omega_{LH}^2}{\Omega_i^4} D_{IM}. \tag{10}$$

This indicates that instabilities occur for $D_{IM} < 0$. We define the imaginary frequency $\omega_i$ of the LHW instabilities as

$$\frac{\omega_i}{\Omega_i} = \begin{cases} \sqrt{\dfrac{1}{1 + \omega_{pe}^2/\Omega_e^2} \dfrac{\omega_{ph}^2 \omega_{LH}^2}{\Omega_i^4} (-D_{IM})} & (D_{IM} < 0) \\ 0 & (\text{otherwise}). \end{cases} \tag{11}$$

Figure 1 shows the imaginary frequency $\omega_i$ as a function of the wavenumber $k_\perp$ for three different values of $v_{Th}$. The other parameters are the same as the simulation parameters shown in Sect. 3. This figure shows that the values of $\omega_i$ and $k_\perp$ of the unstable mode depend on $v_{Th}$. As $v_{Th}$ becomes large, the imaginary frequency decreases and the wavenumber region of the unstable mode becomes wider. When $v_{Th} = 0.1u_\perp$, all the modes of $k_\perp v_A/\Omega_i > 20$ are unstable, which is different from when $v_{Th} = 0.01u_\perp$ and $0.05u_\perp$.

We can roughly estimate the wavenumber of the most unstable mode, which we call $k_m$, from the perpendicular velocity distribution $f_{h\perp}$ as follows. First, we define the velocity where $\partial f_{h\perp}/\partial v_\perp$ is maximum as $V_{gm}$. From Eq. (7), we see that the particles with $v_\perp \simeq V_{gm}$ contribute most significantly to the instabilities. Therefore, we can roughly represent $\epsilon_h$ as

$$\epsilon_h \propto \left.\frac{\partial f_h}{\partial v_\perp}\right|_{v_\perp = V_{gm}} J_n^2\left(\frac{k_\perp V_{gm}}{\Omega_i}\right), \tag{12}$$

where we take only the velocities near $v_\perp \simeq V_{gm}$ into account in the integration in Eq. (7). Because $J_n^2(\xi)$ is the maximum for $\xi \sim n$, $\epsilon_h$ becomes the maximum for $k_\perp V_{gm}/\Omega_i \sim n$. Thus,

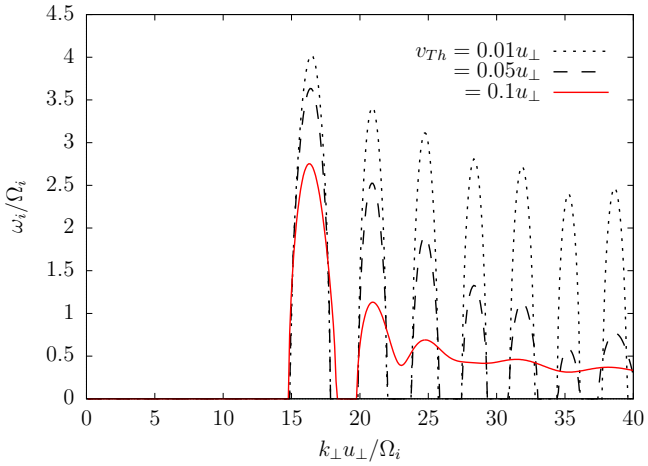


**Fig. 1.** (Color online) Imaginary frequency given by Eq. (11) as a function of the wavenumber $k_\perp$. The three cases for the different thermal velocities of energetic ions, $v_{Th} = 0.01u_\perp$ (dotted line), $v_{Th} = 0.05u_\perp$ (dashed line), and $v_{Th} = 0.1u_\perp$ (red solid line), are plotted, where $u_\perp$ is the ring speed of the energetic ions. Other parameters will be shown in the next section.

we can estimate the wavenumber of the most unstable mode as

$$k_m \sim n\frac{\Omega_i}{V_{gm}} \simeq \frac{\omega_{LH}}{V_{gm}}. \tag{13}$$

Using the parameters for Fig. 1, we obtain $V_{gm} = 0.9u_\perp$ and $k_m \simeq 16\Omega_i/u_\perp$ when $v_{Th} = 0.1u_\perp$. This value of $k_m$ is in good agreement with the wavenumber of the most unstable mode in Fig. 1.

## 3. Simulation Method and Parameters

We study the LHW instabilities by using the one-dimensional (one space and three velocity components) version of the PASTEL code,[26] which self-consistently calculates the full dynamics of electrons and ions and full Maxwell equations. The simulation domain is periodic in the $x$-direction with the length $L_x = 4096\Delta$, where $\Delta$ is the grid separation equivalent to the Debye length. The total number of computational particles is on the order of $10^7$. The plasma consists of three components: electrons, bulk ions, and energetic ions.

The ion-to-electron mass ratio is $m_i/m_e = 1000$, and the ratio of the electron plasma frequency to the electron cyclotron frequency is $\omega_{pe}/\Omega_e = 0.5$. For these values, the lower hybrid resonance frequency defined by Eq. (1) is $\omega_{LH} \simeq 14.2\Omega_i$. The plasma beta is $\beta \simeq 1.0 \times 10^{-2}$. The velocity distributions of the bulk ions and the electrons are Maxwellian with their temperature ratio of $T_i/T_e = 0.2$. The energetic ions have the ring-like velocity distribution given by Eq. (3). The perpendicular ring speed of the energetic ions is $u_\perp = 0.3v_A \simeq 10v_{Th}$, where $v_A$ is the Alfvén speed, and $v_{Th}$ is the thermal velocity of the energetic ions. We set $v_{Th}$

equal to the bulk-ion thermal speed.

In this paper, we investigate the long-time evolution of the instabilities up to the time $\Omega_i t \simeq 80$ with the time step $\Omega_e \Delta t = 0.125$. We compare the simulation results of an initial value problem and an injection model. In the initial value problem, the density ratio of the energetic ions to the bulk ions is constant, $n_h/n_i \simeq 0.02$, throughout the simulation. On the other hand, in the injection model, the energetic-ion density is zero at $\Omega_i t = 0$ and then increases with time. The energetic-ion density at the final time ($\Omega_i t \simeq 80$) is $n_h/n_i \simeq 0.04$, which is twice as large as that in the initial value problem; the time-averaged density is the same between the two models. In the injection model, additional electrons are also injected to maintain the charge neutrality. Both the positions and phases of the energetic ions and the additional electrons are given at random.

We simulate the waves propagating exactly perpendicular to the magnetic field, setting the background magnetic field as $\boldsymbol{B} = (0, 0, B_0)$ and the wavenumber vector as $\boldsymbol{k} = (k_x, 0, 0)$. Landau damping and cyclotron damping of the waves do not occur.

For the simulation parameters, the energy loss time of the energetic ions owing to collisions with the bulk ions or the electrons obtained by the formula in Ref. 27). about $10^4$ times as long as the ion cyclotron period. Therefore, the collisional effects can be neglected in our simulations for the period up to $\Omega_i t \simeq 80$.

## 4. Simulation Results

### *4.1 Initial value problem*

First, we show the simulation results of the initial value problem. Figure 2 shows the amplitudes of the magnetic field fluctuations (left panels) and the electric field fluctuations (right panels) as functions of the wavenumber $k_x$ and the frequency $\omega$. Because we use the Gaussian cgs unit in this paper, the magnetic and electric fields normalized by the background magnetic field are both dimensionless quantities. The upper panels are obtained from the data for the period $0 \leq \Omega_i t \leq 20$. We see that the waves with $\omega \simeq \omega_{LH}$ in the wavenumber region of $50 < k_x v_A/\Omega_i < 90$ have large amplitudes. These waves are LHWs excited by the ring-like energetic ions, and their electric field fluctuations are much stronger than their magnetic field fluctuations. The LHW amplitudes in the lower panels for the period $60 \leq \Omega_i t \leq 80$ are smaller than those in the upper panels for $0 \leq \Omega_i t \leq 20$.

Figure 3(a) shows the time evolution of the electric field fluctuations for four wavenumbers $k_x v_A/\Omega_i = 58, 60, 67$, and 80. The two modes with $k_x v_A/\Omega_i = 58$ (black line) and 60 (red line) grow rapidly at the initial stage. They become saturated at $\Omega_i t \simeq 12$ and are then

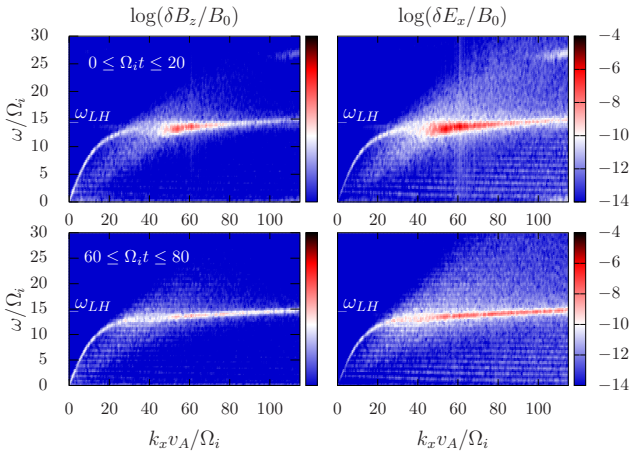


**Fig. 2.** (Color online) Amplitudes of the magnetic field (left panels) and electric field (right panels) fluctuations as functions of the wavenumber $k_x$ and the frequency $\omega$. The color indicates the amplitudes of the fluctuations. Because we use the Gaussian cgs unit in this paper, the magnetic and electric fields normalized by the background magnetic field are both dimensionless quantities. The horizontal axis $k_x$ and the vertical axis $\omega$ are normalized by $\Omega_i/v_A$ and $\Omega_i$, respectively. The upper and lower panels are for the periods $0 \leq \Omega_i t \leq 20$ and $60 \leq \Omega_i t \leq 80$, respectively.

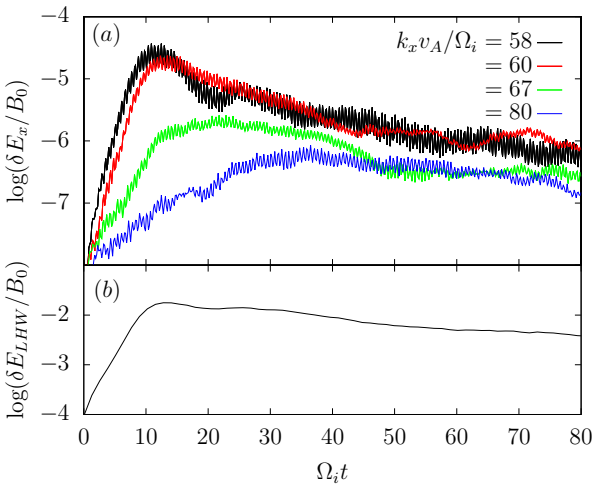


**Fig. 3.** (Color online) Time evolution of the electric field fluctuations for four wavenumbers $k_x v_A/\Omega_i = 58, 60, 67$, and 80 (a) and the intensity of the LHWs integrated over the wavenumber region $0 < k_x v_A/\Omega_i < 115$ (b) in the initial value problem.

gradually damped. Compared with these two modes, the modes with $k_x v_A/\Omega_i = 67$ (green line) and 80 (blue line) grow slower and become saturated at later times. Although there are such differences, all the four modes are gradually damped after the saturation. Figure 3(b)

shows the intensity of the LHWs integrated over the wavenumber, which is defined as

$$\delta E_{\rm LHW} \equiv \int_0^{k_{max}} dk \int_{0.9\omega_{LH}}^{1.1\omega_{LH}} d\omega E_x(k,\omega), \tag{14}$$

where the maximum wavenumber is $k_{max}v_A/\Omega_i = 115$. The peak time of $\delta E_{\rm LHW}$ at $\Omega_i t \simeq 12$ is in good agreement with those of the most unstable modes $k_x v_A/\Omega_i = 58$ and 60, and $\delta E_{\rm LHW}$ is also gradually damped after the saturation.

The time variations of the electric field fluctuations can be roughly explained by the behavior of the energetic-ion velocity distribution and the linear theory presented in Sect. 2. Figure 4 shows snapshots of the energetic-ion perpendicular velocity distribution (left panel) and the imaginary frequency $\omega_i$ of the LHWs given by Eq. (11) (right panel) at $\Omega_i t \simeq 1.3$, 10, and 40. Here, the imaginary frequency is calculated by substituting the $f_{h\perp}$ values observed in the simulation into Eq. (11). At almost the initial time $\Omega_i t \simeq 1.3$, the gradient of $f_{h\perp}$ is very large, and the modes of the wavenumber region $50 \le k_x v_A/\Omega_i \le 60$ are strongly unstable. In Fig. 3, the initial growth rates of the modes $k_x v_A/\Omega_i = 58$ and 60 are both $\gamma \simeq 0.35\Omega_i$, which is about one-third of the imaginary frequency of these modes, $\omega_i \simeq 1.0\Omega_i$, in Fig. 4. At $\Omega_i t \simeq 12$, the $\omega_i$ values of these modes become smaller, and the larger wavenumber modes in the region $70 \le k_x v_A/\Omega_i \le 85$ become more unstable, which is consistent with the mode evolution shown in Fig. 3(a). At $\Omega_i t \simeq 40$, even the larger wavenumber modes have smaller but positive $\omega_i$. This indicates that the larger wavenumber modes can grow even after $\Omega_i t \simeq 40$, which is different from the mode evolution in Fig. 3(a) where all the modes are gradually damped. The reason for this inconsistency will be discussed in Sect. 4.3.

Here, we mention that the waves with $\omega \sim 2\omega_{LH}$ and small amplitudes are also excited (see the wavenumber region $k_x v_A/\Omega_i \simeq 110$ in Fig. 2). They are seemingly the second harmonics of the LHWs. Although the similar waves were observed in the previous simulation studies,[7,19,20,28] we do not discuss the harmonics of the LHWs in this paper. Energetic-ion injection effects on the harmonics of the LHWs will be our future work.

### *4.2 Injection model*

In this subsection, we show the simulation results of the injection model. We found that the development of the LHWs excited by the ring-like energetic ions in the injection model is quite different from that in the initial value problem. Figure 5 shows the amplitudes of the electric field and the magnetic field fluctuations in the injection model for the periods $0 < \Omega_i t < 20$, $20 < \Omega_i t < 40$, and $40 < \Omega_i t < 60$. Comparing the top panels of Fig. 5 and of Fig. 2, we see that the initial excitation of the LHWs is localized in the narrow wavenumber

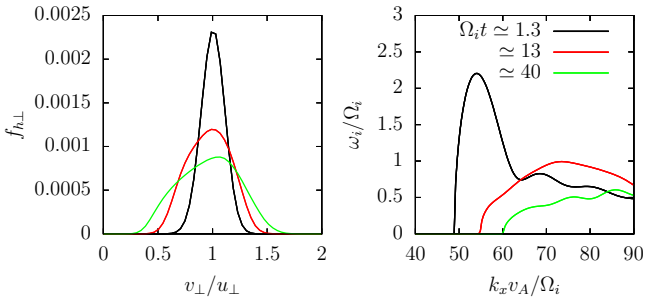


**Fig. 4.** (Color online) Snapshots of the perpendicular velocity distributions at $\Omega_i t \simeq 1.3$ (black line), 12 (red line), and 40 (green line) (left panel) and the corresponding values of the imaginary frequency defined by Eq. (11) (right panel) in the initial value problem.

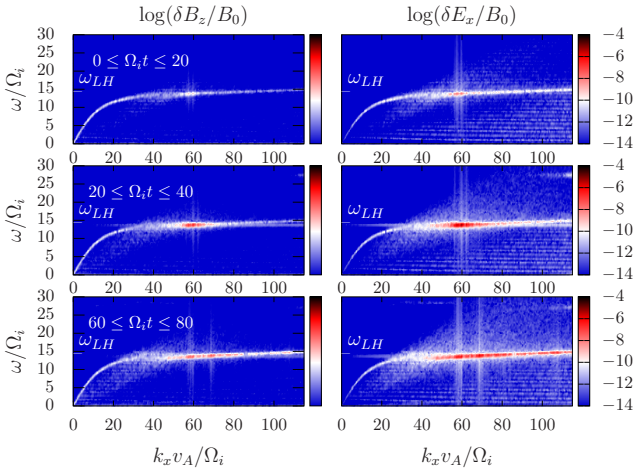


**Fig. 5.** (Color online) Amplitudes of the magnetic and electric field fluctuations in the injection model (same format as in Fig. 2).

region near $k_x v_A/\Omega_i = 60$ in the injection model. This is because the limited modes can grow owing to the lack of the energetic ions in the initial stage. However, in the later periods shown in the middle and bottom panels of Fig. 5, the larger wavenumber modes are excited.

The time variations of the typical four modes are shown in Fig. 6(a). Unlike in the initial value problem where all the modes are gradually damped after the saturation, the mode development in the injection model strongly depends on the wavenumber $k_x$. The mode $k_x v_A/\Omega_i = 60$ (red line) is damped after $\Omega_i t \simeq 26$. However, the mode $k_x v_A/\Omega_i = 58$ (black line) maintains its large amplitude even after this time. The modes $k_x v_A/\Omega_i = 67$ (green) and 80 (blue) continue to grow for a long period, although they are excited later than the modes $k_x v_A/\Omega_i = 58$ and 60. Figure 6(b) shows that the LHW intensity $\delta E_{\rm LHW}$ given by Eq. (14) continues to gradually increase even after $\Omega_i t \simeq 26$, although there is a small fluctuation.

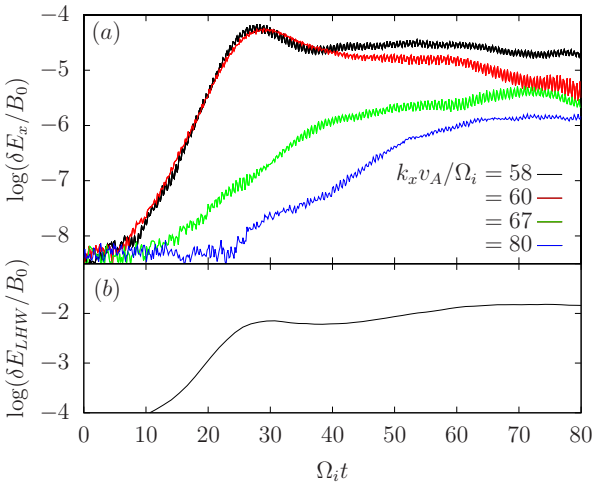


**Fig. 6.** (Color online) Time evolution of the electric field fluctuations (same format as in Fig. 3).

This is quite different from the initial value problem where $\delta E_{\rm LHW}$ gradually decreases after its saturation. These results indicate that the energetic-ion injection plays an essential role in destabilizing the LHW modes.

Figure 7 shows snapshots of the energetic-ion perpendicular velocity distribution $f_{h\perp}$ in the injection model (red line) at four different times. For comparison, $f_{h\perp}$ in the initial value problem (black line) is plotted. At almost the initial time $\Omega_i t \simeq 1.3$, $f_{h\perp}$ of the injection model is almost equal to that of the initial value problem, although the total number of energetic ions in the injection model is quite small. The $f_{h\perp}$ of the injection model maintains its shape at $\Omega_i t \simeq 12$ around which the LHWs begin to grow (see Fig. 6). The shape of $f_{h\perp}$ collapses by $\Omega_i t \simeq 26$, as shown in the lower panels where the maximum value for the vertical axis is about 5% of that of the upper panels. This time is in good agreement with the time when the rapid increase in $\delta E_{\rm LHW}$ ends [see Fig. 6(b)]. At this time and $\Omega_i t \simeq 40$, $f_{h\perp}$ of the injection model has the steeper gradient than $f_{h\perp}$ of the initial value problem. Both in the initial value problem and in the injection model, the values of $V_{gm}$, where $\partial f_{h\perp}/\partial v_\perp$ becomes maximum, decreases with time through wave-particle interactions. The vertical dashed lines in Fig. 7 represent $V_{gm}$ in the injection model, and the values of $V_{gm}/u_\perp$ at $\Omega_i t \simeq 12, 26$, and 40 are 0.89, 0.70, and 0.58, respectively. Owing to the decrease in $V_{gm}$ with time, the wavenumber of the most unstable mode, $k_m$, becomes large, as expected from Eq. (13). Moreover, note that the energetic-ion injection can make $\partial f_{h\perp}/\partial v_\perp$ greater and prevent excited waves from being damped, which is different from the initial value problem. As a result, broadband LHWs can be excited in the injection model, as shown in Fig. 6.

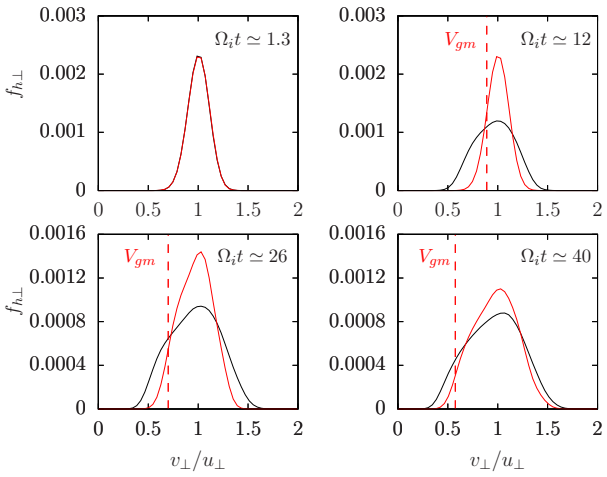


**Fig. 7.** (Color online) Snapshots of the perpendicular velocity distribution for the injection model (red line) at four different times The horizontal axis indicates the perpendicular velocity normalized by the ring speed $u_\perp$, and the vertical axis indicates the perpendicular velocity distribution. The perpendicular velocity distribution for the initial value problem is also plotted for comparison (black line). Vertical dashed lines represent $V_{gm}$ in the injection model.

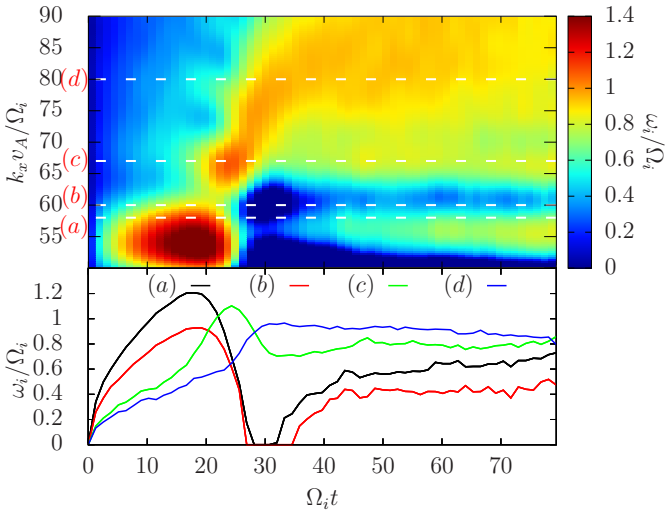


**Fig. 8.** (Color online) Time evolution of the imaginary frequency in the injection model. In the upper panel, the horizontal and vertical axes indicate the simulation time and the wavenumber, respectively, and the color indicates the value of the imaginary frequency $\omega_i$ of the LHWs given by Eq. (11). Lines labeled (a)–(d) indicate the wavenumbers of the modes shown in Fig. 6, $k_x v_A/\Omega_i = 58, 60, 67$, and 80. The imaginary frequencies of each mode are plotted in the lower panel.

We investigate the relationship between the evolution of the electric field fluctuations and the LHW imaginary frequency $\omega_i$ given by the linear theory. Figure 8 shows $\omega_i$ as a function of the simulation time and the wavenumber, where we obtained $\omega_i$ by substituting

$f_{h\perp}$ observed in the simulation into Eq. (11). The color shows the value of $\omega_i$. Focusing on the region colored red, we see that the wavenumber region of the most unstable modes is $50 < kv_A/\Omega_i < 60$ in the initial stage $0 < \Omega_i t < 26$. After $\Omega_i t \simeq 26$, the region of the most unstable mode shifts to the larger wavenumber region over time. This is qualitatively consistent with the evolution of the electric field fluctuations shown in Figs. 5 and 6.

We compare in detail the time evolution of the four modes in Fig. 6(a) with that in Fig. 8 where the four mode wavenumbers are shown by the white dashed lines labeled (a)–(d). The development of the instabilities in the injection model cannot be completely explained by $\omega_i$ given by Eq. (11) where the time development of $f_{h\perp}$ and the density variation of the energetic ions are not considered. For example, the $\omega_i$ values are much larger than the mode growth rates observed in the simulation, and some modes do not grow even if their $\omega_i$ values are positive. However, we find that Eq. (11) is still useful to qualitatively understand the differences between the modes.

We first consider modes (a) and (b). In Fig. 6, these modes start to grow rapidly at $\Omega_i t \simeq 10$ and become saturated at $\Omega_i t \simeq 26$. The growth rates of modes (a) and (b) in this period are $\gamma \simeq 0.23\Omega_i$ and $0.20\Omega_i$, respectively. On the other hand, the time-averaged $\omega_i$ values of these modes in Fig. 8 are $1.1\Omega_i$ and $0.8\Omega_i$, respectively. Although there is a quantitative gap between the simulation and theory, they have the common fact that the growth rate of mode (a) is larger than that of mode (b). After $\Omega_i t \simeq 26$, the two modes become almost zero in $\omega_i$ in Fig. 8 and decrease in amplitude in Fig. 6. After $\Omega_i t \simeq 40$ in Fig. 8, the $\omega_i$ value of the mode (a) continues to increase and is larger than that of mode (b). This can be responsible for the fact that mode (a) maintains its amplitude whereas mode (b) is gradually damped in Fig. 6. We next consider modes (c) and (d). According to Fig. 8, the $\omega_i$ values of modes (c) and (d) become large at $\Omega_i t \simeq 15$ and 25, respectively. These times are almost equal to the time when modes (c) and (d) begin to grow, respectively, as shown in Fig. 6(a). As time advances, the values of $\omega_i$ gradually decrease and the growth rates of modes (c) and (d) become lower.

Thus, we have confirmed that the development of the LHW modes is closely related to the evolution of the velocity distribution of the energetic ions continuously injected into the plasma. However, we find that the LHW development cannot be completely explained by the linear theory. For example, mode (a) does not grow when the period $\Omega_i t > 40$ [see Fig. 6(a)], although $\omega_i$ for this period is positive (Fig. 8). This indicates that nonlinear effects become important, which we discuss below.

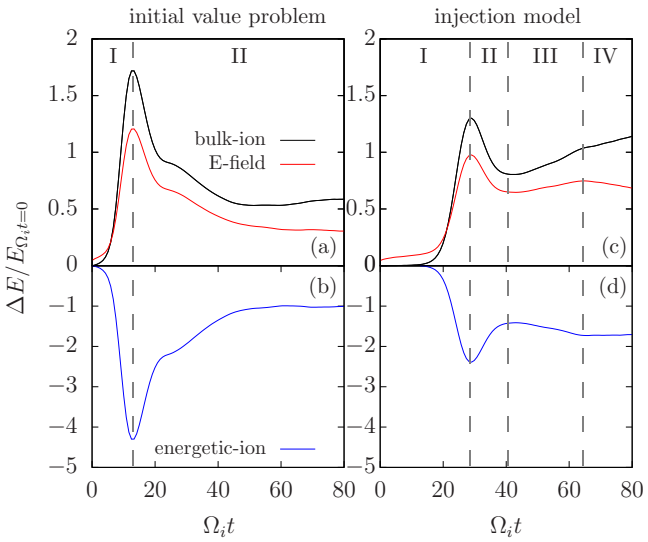


**Fig. 9.** (Color online) Time evolution of total energies for bulk ions, electric fields (upper panels) and energetic ions (lower panels). The changes from their initial values are plotted. Roman numerals I to IV denote the periods of instability development (see Fig. 10).

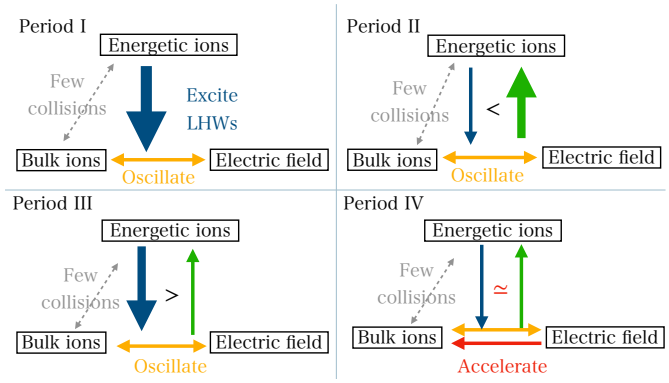


**Fig. 10.** (Color online) Illustration of instability development. The direction and size of arrows indicate the direction and level of energy transfer. In the initial value problem, Periods I and II are observed. However, in the injection model, Periods I to IV can be observed owing to the continuous injection of the energetic ions.

### *4.3 Energy transfer*

In this subsection, we investigate energy transfer among the electric field, the bulk ions, and the energetic ions in association with the development of the LHW instabilities. We found that the energetic-ion injection can significantly enhance the energy transfer from the energetic ions to the bulk ions.

Figure 9 shows the time evolution of total energies for bulk ions, electric fields (upper panels) and energetic ions (lower panels). Here, the changes from their initial values are plotted. The energy changes in the initial value problem are shown in Figs. 9(a) and 9(b) and

those in the injection model are shown in Figs. 9(c) and 9(d) where the net energy change of the energetic ions is plotted. The net change means the difference between the total energetic-ion energy at a given time $t$ and the total injected energy of energetic ions by the time $t$. The energy changes of the electron and the magnetic field are not plotted because they are negligibly small compared with the energy changes of the bulk ion and the electric field. Therefore, the sum of the bulk-ion energy, the electric field energy, and the net energy change of the energetic ions is almost constant.

In the initial value problem in Figs. 9(a) and 9(b), the time evolution of the bulk-ion energy is quite similar to that of the electric field energy, indicating that the bulk ions oscillate in the LHWs excited by the energetic ions. This is the case for the injection model for the period $0 < \Omega_i t < 60$ in Figs. 9(c) and 9(d). However, after $\Omega_i t \simeq 60$, the time evolution of bulk-ion energy is different from that of the electric field energy, and the energy is transferred from the electric field to the bulk ions. This indicates that the bulk ions are effectively accelerated by the LHWs.

We now consider the time variations in detail. We found that the nonlinear development of the instabilities can be illustrated as shown in Fig. 10. Figure 9 shows that in the initial stage $\Omega_i t < 12$ of the initial value problem, the energy is transferred from the energetic ions to the electric field and the bulk ions by the excitation of LHWs. We call this stage Period I, as shown in Fig. 10. After $\Omega_i t > 12$, the energetic-ion energy increases whereas the bulk-ion and the electric field energies decrease. This indicates that the energy is transferred from the LHWs to the energetic ions. Because of this energy transfer, all the wavenumber modes in Fig. 3 are damped, although these modes have the positive $\omega_i$ based on the linear theory in Fig. 4. We call this nonlinear stage Period II. Although the time evolution cannot be explained by the linear theory, we find that the relationship between the energies of the bulk ions and the electric field can be described by the linear theory based on the two-fluid model,

$$\frac{1}{2} n_i m_i V_x^2 = \left( \frac{\omega_{pi}}{\omega_{LH}} \right)^2 \frac{E_x^2}{8\pi}, \tag{15}$$

where $n_i$ is the bulk-ion density, $V_x$ is the bulk-ion fluid speed, and $\omega_{pi}^2/\omega_{LH}^2 \simeq 1.25$ for the simulation parameters. Therefore, we see that the bulk ions are oscillating in the LHWs even in Period II.

Regarding the injection model, Periods I and II correspond to the periods $0 < \Omega_i t < 26$ and $26 < \Omega_i t < 40$, respectively. Furthermore, in the injection model, other stages appear, which we call Periods III and IV. In Period III, which corresponds to $40 < \Omega_i t < 65$, the amount of energy transfer from the energetic ions to the LHWs is greater than that of the

reverse energy transfer. Therefore, the energetic-ion energy decreases and the LHW energy increases. As shown in Fig. 6, the broadband wavenumber modes are growing in Period III. In Period IV ($\Omega_i t > 65$), the amount of energy transfer from the energetic ions to the LHWs is almost equal to that of the reverse energy transfer. Moreover, we note that the bulk-ion energy increases as the electric field energy decreases, which is not observed in Period I, II, or III. This indicates that the energy is transferred from the electric field to the bulk ions in Period IV. This bulk-ion acceleration mechanism is not due to Landau damping or cyclotron damping because we consider the waves propagating exactly perpendicular to the magnetic field. In the next subsection, we discuss the bulk-ion acceleration mechanism in Period IV.

## 5. Dependence of Energy Transfer on the Energetic-ion Injection Speed

In this section, we discuss how the nonlinear development of the instabilities depends on the energetic-ion injection speed. Figure 11 shows the time evolution of total bulk-ion energy and total electric field energy for the two different energetic ion speeds $S_{inj} = 0.5$ and 2.0, where $S_{inj} = 1.0$ is the injection speed described in Sect. 3 and used in Sect. 4.2. For $S_{inj} = 2.0$ and 0.5, the energetic ions are injected twice and half as fast as in the case of $S_{inj} = 1.0$, respectively. For $S_{inj} = 0.5$, Periods I, II, and III are observed, but we cannot see Period IV in this case. The energy increase of the bulk ions for $S_{inj} = 0.5$ is smaller than that for $S_{inj} = 1.0$. On the other hand, in the case of $S_{inj} = 2.0$, Period IV begins at $\Omega_i t \simeq 50$, which is faster than the start time of Period IV in the case of $S_{inj} = 1.0$. The energy increase of the bulk ions in Period IV for $S_{inj} = 2.0$ is about twice that for $S_{inj} = 1.0$. We find that the bulk-ion acceleration is enhanced as the energetic-ion injection speed increases.

Figure 12 shows wavenumber spectra of the electric field fluctuations for $S_{inj} = 0.5$ (blue line), $S_{inj} = 1.0$ (black line), and $S_{inj} = 2.0$ (red line). These electric field fluctuations are excited by the ring-like energetic ions continuously injected into the plasma, as described in Sect. 4.2. The upper panel (a) shows the amplitudes at the end time of Period II for the cases of $S_{inj} = 0.5$, 1.0, and 2.0. We see that as $S_{inj}$ becomes larger, the amplitudes become slightly larger over a wide wavenumber region.

The lower panel (b) shows the amplitudes of the electric field fluctuations at the end of the simulation $\Omega_i t = 80$. As a result of nonlinear evolution, these fluctuations are excited. This figure clearly shows that more broadband wavenumber modes are excited as $S_{inj}$ increases. Although not shown in this paper, we also performed the simulation of $S_{inj} = 0.5$ for a longer time $\Omega_i t \simeq 160$ and observed that even when $S_{inj} = 0.5$, the longer energetic-ion injection causes the excitation of the broadband wavenumber modes and associated ion acceleration.

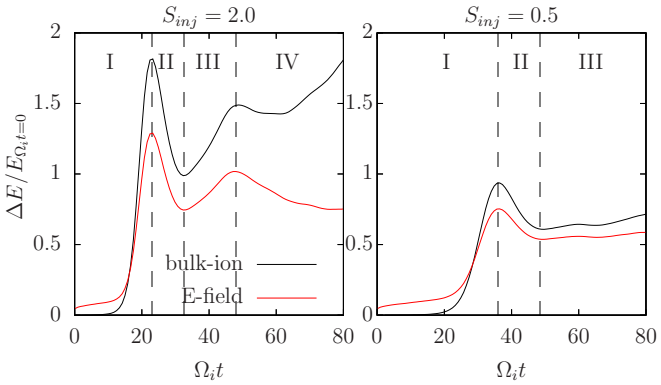


**Fig. 11.** (Color online) Time evolution of total bulk-ion energy and total electric field energy for $S_{inj} = 2.0$ (left panel) and $S_{inj} = 0.5$ (right panel) (same format as in the upper panels in Fig. 9).

Therefore, we have concluded that the bulk-ion acceleration in Period IV is caused by the broadband wavenumber modes. This mechanism can be a type of ion acceleration by LHW turbulence.[29)]

Figure 13 shows the profiles of $\partial f_{h\perp}/\partial v_\perp$ as a function of $v_\perp$ at four different times for $S_{inj} = 1.0$ and $S_{inj} = 2.0$, and the dashed-colored lines indicate $V_{gm}$ where $\partial f_{h\perp}/\partial v_\perp$ is the maximum for each case. Comparison of the $V_{gm}$ values between $S_{inj} = 1.0$ and 2.0 at the same time shows that $V_{gm}$ for $S_{inj} = 2.0$ is clearly smaller than that for $S_{inj} = 1.0$. This indicates that the velocity distribution is quickly changed by the faster energetic-ion injection. This difference causes the wider wavenumber spectra for $S_{inj} = 2.0$ than for $S_{inj} = 1.0$, as shown in Fig. 12.

We also performed the simulations for $S_{inj} = 0.3$ and 1.5 and show the results in Fig. 14. The bulk-ion energy increase normalized by the initial energy is plotted as a function of the injection speed $S_{inj}$. The black and red circles denote the values at the end time of Period II and at the simulation final time $\Omega_i t = 80$, respectively. That is, the difference between the black and red circles is the energy increase for Periods III and IV, which appears due to the energetic-ion injection. We confirm that the energy increase becomes larger with increasing $S_{inj}$. Furthermore, at $S_{inj} = 1.5$ and 2.0, the energy increase at the final time is much greater than that at the end time of Period II. This indicates that the bulk-ion acceleration by the broadband wavenumber modes becomes important when $S_{inj}$ is large.

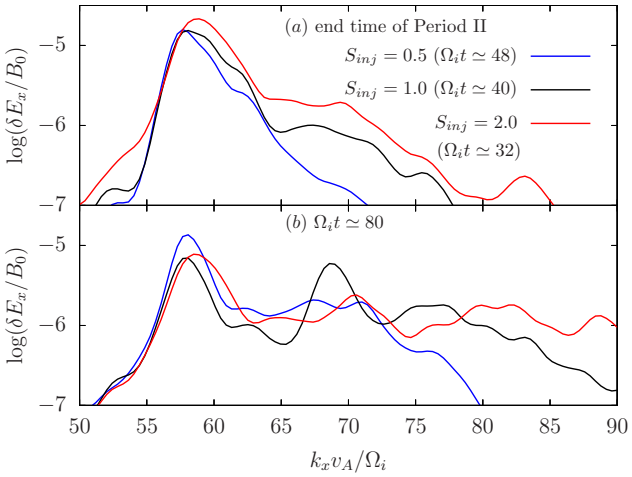


**Fig. 12.** (Color online) Wavenumber spectra of the electric field fluctuations for $S_{inj} = 0.5$ (blue line), $S_{inj} = 1.0$ (black line), and $S_{inj} = 2.0$ (red line). Upper panel (a) shows the spectra at the end time of Period II (see Figs. 10 and 11) and lower panel (b) shows the spectra at the final time of the simulations $\Omega_i t \simeq 80$.

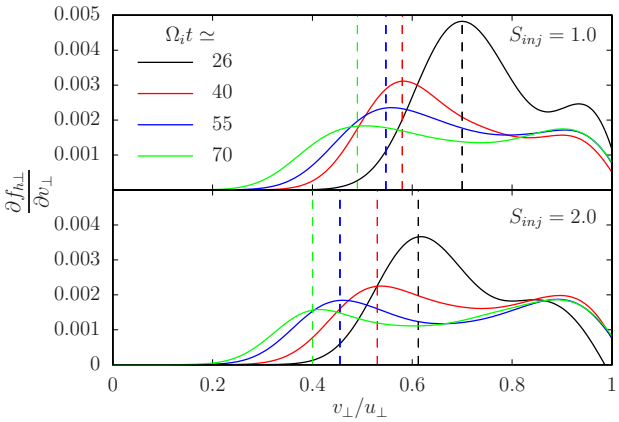


**Fig. 13.** (Color online) Snapshots of the gradient of $\partial f_{h\perp}/\partial v_\perp$ for $S_{inj} = 1.0$ and 2.0 for each time. Dashed-colored lines indicate $V_{gm}$ for each case.

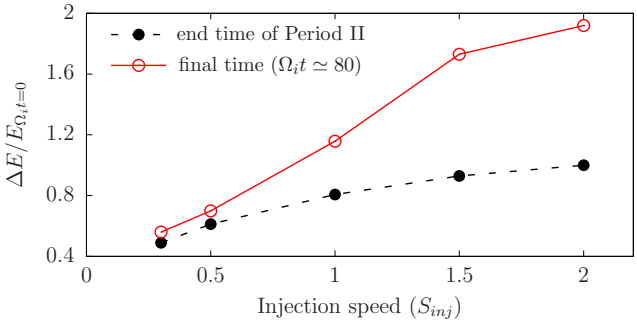


**Fig. 14.** (Color online) Dependence of the energy increase of bulk ions on the energetic-ion injection speed. The black and red circles denote the values at the end of Period II and at the simulation final time $\Omega_i t \simeq 80$, respectively.

## 6. Summary and Discussion

By means of one-dimensional, electromagnetic, particle-in-cell simulations, we have investigated the LHW instabilities driven by the ring-like energetic ions, paying special attention to the effect of the continuous energetic-ion injection. We have shown that the energetic-ion injection affects the excitation of the LHWs, the nonlinear development of the LHWs, and the energy transfer from the energetic ions to the bulk ions through the LHWs.

In the initial value problem, all the LHWs excited by the energetic ions are gradually damped after their saturation. However, in the injection model, the LHWs excited by the energetic ions can maintain large amplitudes for a long time. Moreover, the large wavenumber modes are excited as time advances. This is because the continuous injection causes the steep gradient of the energetic-ion velocity distribution. As a result of the excitation of the wide wavenumber modes, the energy transfer from the energetic ions to the bulk ions is enhanced. As the injection speed increases, the wide wavenumber modes are excited and the bulk-ion energy change increases. The bulk-ion acceleration mechanism can be turbulent heating by the LHWs, because we consider the waves propagating exactly perpendicular to the magnetic field, and the Landau damping and cyclotron damping do not occur.

In this paper, we consider the LHWs excited by energetic ions with a speed smaller than the Alfvén speed. The LHWs are electrostatic waves. If the energetic-ion speed is comparable to or larger than the Alfvén speed, the electromagnetic waves can be excited. It is important to study the effect of energetic-ion injection on the nonlinear development of the electromagnetic waves and associated energy transfer.

To investigate the nonlinear development of the instabilities for a much longer time, we have to take into account the loss of the energetic ions, which are not considered in this study. In the near future, we will make a model including both the injection and the loss of the energetic ions and study the effects of energetic-ion loss.

**Acknowledgments** This work is performed on “Plasma Simulator” (NEC SX-Aurora TSUBASA) of NIFS with the support and under the auspices of the NIFS Collaboration Research program (NIFS21KNSS164 and NIFS20KNSS151). This work was supported in part by “Joint Usage/Research Center for Interdisciplinary Large-scale Information Infrastructures” in Japan (Project ID: jh1900007-NAH).

## References


1) N. Sckopke, G. Paschmann, A. L. Brinca, C. W. Carlson, and H. Luhr, J. Geophys. Res. **88**, 6121 (1983).

2) L. Chen, R. M. Thorne, V. K. Jordanova, M. F. Thomsen, and R. B. Horne, J. Geophys. Res. **116**, 03223 (2011).

3) A. Mikhailovskii, *Theory of Plasma Instabilities* (Consultants Bureau, New York, 1974), Vol. 1.

4) O. Santolík, F. Němec, K. Gereová, E. Macúšová, Y. de Conchy, and N. Cornilleau-Wehrlin, Ann. Geophys. **22**, 2587 (2004).

5) R.B. Horne, R. M. Thorne, S. A. Glauert, N. P. Meredith, D. Pokhotelov, and O. Santolík, Geophys. Res. Lett. **34**, L17107 (2007).

6) K. Liu, S. P. Gary, and D. Winske, J. Geophys. Res. **116**, A07212 (2011).

7) J. Sun, X. Gao, Q. Lu, L. Chen, X. Tao, and S. Wang, Phys. Plasma **23**, 022902 (2016).

8) J. Sun, X. Gao, Q. Lu, L. Chen, X. Liu, X. Wang, X. Tao, and S. Wang, J. Geophys. Res. **122**, 5377 (2017).

9) Z. Yuan, X. Yu, S. Huang, Z. Qiao, F. Yao, and H. O. Funsten, J. Geophys. Res. **123**, 1242 (2018).

10) S. Hill, N. Buzulukova, S. Boardsen, and M. -C. Fok, J. Geophys. Res. **125** (2020).

11) K. Akimoto, K. Papadopulos, and D. Winske, J. Plasma Phys. **34**, 445 (1985).

12) M. Toida, K. Saito, H. Igami, T. Akiyama, S. Kamio, and R. Seki, Plasma Fusion Res. **13**, 3403015 (2018).

13) K. Saito, H. Igami, M. Toida, T. Akiyama, S. Kamio, R. Seki, and L. E. Group, Plasma and Fusion Res. **13**, 3402043 (2018).

14) X. Liu, L. Chen, and Q. Ma, Geophys. Res. Lett. **48** (2021).

15) K. G. McClements, J. J. S. R. Bingham, J. M. Dawson, and D. S. Spicer, Solar Phys. **130**, 229 (1990).

16) K. G. McClements, R. Bingham, J. J. Su, J. M. Dawson, and D. S. Spicer, Astrophys. J. **409**, 465 (1993).

17) R. Bingham, J. M. Dawson, and V. D. Shapiro, J. Plasma Phys. **68**, 161 (2002).

18) M. André, P. Norqvist, L. Andersson, L. Eliasson, A. I. Eriksson, L. Blomberg, R. E. Erlandson, and J. Waldemark, J. Geophys. Res. **103**, 4199 (1998).

19) X. Gao, J. Sun, Q. Lu, L. Chen, and S. Wang, Geophys. Res. Lett. **45**, 8029 (2018).

20) B. Chapman, R. O. Dendy, S. C. Chapman, K. G. McClements, G. S. Yun, S. G. Thatipamula, and M. H. Kim, Nucl. Fusion **58**, 096027 (2018).

21) D. Winske and W. Daughton, Phys. Plasma **19**, 072109 (2012).

22) D. Winske and W. Daughton, Phys. Plasma **22**, 022102 (2015).

23) B. Eliasson and K. Papadopoulos, J. Geophys. Res. **113**, A09315 (2008).

24) E. Camporeale, G. L. Delzanno, and P. Colestock, J. Geophys. Res. **117**, A10315 (2012).

25) X. Li, D. N. Baker, S. Elkington, M. Temerin, G. D. Reeves, R. D. Belian, J. B. Blake, H. J. Singer, W. Peria, and G. Parks, J. Atmos. Sol. Terr. Phys. **65**, 233 (2003).

26) T. Moritaka, Y. Kuramitsu, Y. L. Liu, and S. H. Chen, Phys. Plasma **23**, 032110 (2016).

27) J. D. Huba, *NRL Plasma Formulary* (Naval Research Laboratory, Washington, D.C., 2013).

28) K. Min and L. Kaijun, J. Geophys. Res. **120**, 2739 (2015).

29) J. B. McBride, E. Ott, J. P. Boris, and J. H. Orens, Phys. Fluids **15**, 2367 (1972).